Temporal Pulse Engineering of Spectral Evolution in a Synthetic Frequency Lattice

Jingkun Zhuang[1], Qunchao Ma[1], Zhenyu Jiang[1], Mingjin Yang[1], Zhuochao Tie[1], Yan Liang[1], Cheng Wang[2*], Songlin Zhuang[1], and Qingqing Cheng[1,2*]

[1]*School of Optical-Electrical and Computer Engineering, University of Shanghai for Science and Technology, Shanghai 200093, China*

[2]*State Key Laboratory of Terahertz and Millimeter Waves, City University of Hong Kong, Hong Kong, China*

(Received 28 May 2025; accepted manuscript online 25 August 2025)

Precise experimental control and characterization of electron wave packet dynamics driven by external optical fields remain a fundamental challenge, particularly at ultrafast temporal and sub-microscopic spatial scales. To overcome these challenges, we introduce a photon-based simulation platform employing a traveling-wave electro-optic phase-modulated waveguide. In our setup, the incident electromagnetic pulse serves as an analog to the electron wave packet, while the traveling-wave modulation simulates the external optical driving field. Our experimental study systematically explores pulse evolution under three distinct regimes defined by the relation between the pulse duration (Δt) and the modulation period (T). When the pulse duration is significantly shorter than the modulation period, we observe a uniform spectral shift analogous to electron acceleration in dielectric laser accelerators, where spectral phase gradients represent electron momentum accumulation. Conversely, when the pulse duration greatly exceeds the modulation period, discrete diffraction patterns emerge, closely resembling the discrete sideband features of electron–photon coupling observed in photon-induced near-field electron microscopy. Notably, in the intermediate regime ($T/4 < \Delta t < T/2$), the pulse spectrum exhibits Airy-function-type characteristics with self-healing effects. These experimental results provide critical insights into electron-wave interactions under external optical fields and establish a robust, programmable framework for further investigation.

DOI: 10.1088/0256-307X/42/10/100404 CSTR: 32039.14.0256-307X.42.10.100404

1. Introduction. Synthetic dimensions in photonics have emerged as a powerful approach to overcoming longstanding challenges in experimental physics.[1–5] By creating artificial dimensions[6–8] that mimic complex interactions usually found in higher-dimensional systems, this technique allows researchers to explore phenomena that are otherwise difficult to observe directly.[9,10] Various physical platforms have successfully demonstrated the concept, including resonant ring structures,[11] coupled waveguide arrays,[12] and spatial modulators[13] that encode new degrees of freedom[14,15] into photons. Of particular interest are the $LiNbO_3$ waveguides,[16–19] which stand out for their dynamic tunability and precise control. In these waveguides, frequency interactions closely mimic electronic behaviors observed in solid-state crystals,[20–25] enabling detailed investigation of electron pulse dynamics.

At a fundamental level, a strong mathematical similarity exists between electron wave packets and pulses of electromagnetic waves. This similarity significantly influences how electrons interact with optical fields, depending largely on the size of the electron wave packet relative to the wavelength of the external field.[26,27] When electron packets are much smaller than the optical wavelength, electrons behave like classical particles and experience momentum shifts akin to acceleration in dielectric laser accelerators (DLA).[28–30] Conversely, if electron packets exceed the optical wavelength—as seen in photon-induced near-field electron microscopy (PINEM)[31–33] and quantum free-electron laser[34] experiments—electrons show quantum behavior, absorbing or emitting discrete amounts of photons. Thus, by adjusting either the electron packet size or the optical wavelength, one can transition seamlessly between particle-like and wave-like electron behavior.[35–37] However, experimentally capturing and controlling these electron dynamics remains challenging due to their extremely short timescales and tiny spatial dimensions, necessitating innovative simulation methods that can offer greater control and insight.

To address these challenges, here we introduce a novel simulation platform based on a dynamically modulated spoof plasmonic waveguide.[38–40] Under an ideal sinusoidal refractive index modulation, we derive a coupled-mode equation based on the tight-binding approximation[41–43] in which only nearest-neighbor modes are coupled and analytically obtain the corresponding band structure. Our approach systematically reveals how incident pulse parameters influence pulse evolution within a synthetic frequency dimension. Numerical analyses show that selectively exciting the number of frequency modes is possible simply by adjusting the inci-

*Corresponding authors. Email: cwang257@cityu.edu.hk; qqcheng@usst.edu.cn

© 2025 Chinese Physical Society and IOP Publishing Ltd. All rights, including for text and data mining, AI training, and similar technologies, are reserved.

dent pulse width. Moreover, we achieve exact control over the distribution of frequency modes by tuning the timing of interactions between the pulses and the modulated wave on the waveguide. Experimentally, we observe three distinct behaviors: uniform spectral shifts occur for short pulse durations (approximately $\Delta t < T/4$), Airy-type spectral profiles emerge at intermediate durations ($T/4 < \Delta t < T/2$), and discrete diffraction patterns appear for longer durations ($\Delta t > T/2$). Our findings offer a deeper theoretical understanding of photon–electron analogies [44,45] and open promising pathways toward advanced applications in integrated photonics, optical communication systems, and hybrid photonic-electronic device technologies.

2. Frequency Evolution of Pulses in a Phase Modulator. A waveguide with a dynamically controlled refractive index is presented in Fig. 1(a). The system functions as a traveling-wave electro-optic phase modulator with the refractive index varying sinusoidally. This variation is expressed as $n(z,t) = n_0 + \Delta n \cos(\Omega t - qz + \phi)$, where n_0 is the background refractive index, Δn is the modulation amplitude, Ω is the modulation frequency, q is the wave vector, and ϕ is the initial phase. The dynamic modulation of the refractive index induces intra-band transitions of the photonic state, resulting in the formation of a discrete frequency lattice. [2,46] The frequencies and propagation constants of each mode are $\omega_n = \omega_0 + n\Omega$ and $k_n = k_0 + nq$, respectively. The newly generated harmonic mode remains a guided wave mode of the waveguide, where $n = 0, \pm1, \pm2, \ldots$ represents the harmonic order, and k_0 is the propagation constant of the carrier frequency ω_0. The propagation of harmonics in the waveguide continues to satisfy the wave equation. Upon discretization, the amplitude of each harmonic mode under sinusoidal modulation adheres to the nearest-neighbor coupled mode equation, [47–50] expressed as:

$$\mathrm{i}\frac{\partial}{\partial z}a_n(z) = -\frac{\omega_0 \Delta n}{2c}[a_{n+1}(z)\mathrm{e}^{\mathrm{i}\phi} + a_{n-1}(z)\mathrm{e}^{-\mathrm{i}\phi}]. \quad (1)$$

Equation (1) generally describes the evolution of the amplitude $a_n(z)$ of discrete frequencies in the waveguide. The equation's solution is detailed in the Supplementary Materials (SM), with the output field given by

$$E_{\mathrm{out}}(t) = \mathrm{e}^{\mathrm{i}m_\varphi \cos(\Omega t - \phi)} E_{\mathrm{in}}(t), \quad (2)$$

where $m_\varphi = \frac{\Delta n \omega_0 z}{c}$ is the modulation depth, c is the speed of light, and z is the propagation length.

The phase modulation term $\mathrm{e}^{\mathrm{i}m_\varphi \cos(\Omega t - \phi)}$ in Eq. (2) generates a frequency comb with an interval of Ω. The product of the phase modulation term and the incident field in the time domain is equivalent to a convolution operation in the frequency domain. Therefore, the relation between the spectral width of the incident pulse and the frequency comb interval Ω directly determines the spectrum envelope. When a pulse with a certain spectral width is fed into the phase modulator, it propagates within the modulated waveguide, traveling along a frequency lattice. If the spectral width of the pulse is less than the modulation frequency interval, as illustrated in Fig. 1(d),

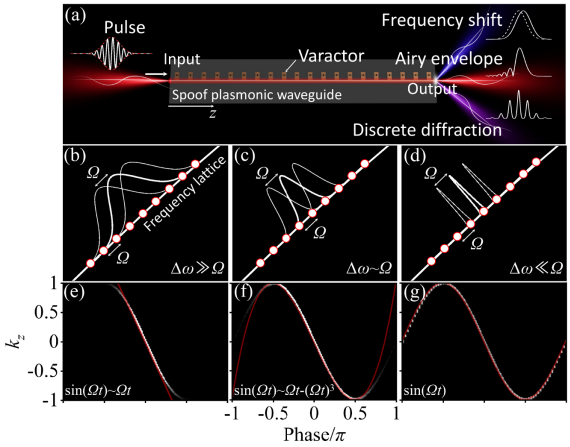

Fig. 1. Schematic of the sample. (a) A pulse incident on the spoof plasmonic waveguide propagates through it, resulting in three distinct spectral envelopes—an overall spectral shift, an Airy-type spectral envelope, and discrete spectral diffraction. (b) The pulse's spectral width covers multiple frequency lattices. (c) The number of frequency lattices is reduced. (d) The frequency lattices are further reduced to a single lattice. Changes to the pulse's spectral width alter the distribution of photonic states within the energy band. (e) Photonic states are confined to the Brillouin center, following a linear relation with Ωt. (f) Photonic states extend beyond the Brillouin center, following a cubic relation, $\Omega t - (\Omega t)^3/6$. (g) Photonic states span the entire energy band, following a sine function, $\sin(\Omega t)$.

the pulses at adjacent sites remain isolated and do not interact. However, if the spectral width exceeds the modulation frequency interval, as illustrated in Fig. 1(c), pulses at adjacent sites overlap and interfere. In cases where the spectral width is extremely large, such that pulses at multiple sites coherently superimpose, as illustrated in Fig. 1(b), the output frequency spectrum exhibits an overall spectral shift. This behavior is analogous to electron acceleration in DLA, where the convolution operation in the frequency domain determines the resulting spectral envelopes, setting the stage for further analysis of the complex interactions within the modulated waveguide.

3. Time-Domain Pulse. Spoof plasmonic waveguides with dynamically modulated refractive indices are implemented, where varactor diodes are discretely positioned along the propagation direction z. By applying a variable voltage to the varactor diodes, their capacitance changes, which in turn modulates the propagation constant of the plasmonic waveguide mode. An arbitrary waveform generator supplies a microwave frequency signal with a varying pulse width to one end of the waveguide. After traversing the modulated waveguide, the signal is analyzed by a spectrum analyzer at the output. In our experiment, the incident spectrum is configured as a continuous Gaussian pulse centered at $\omega_0 = 2.4\,\mathrm{GHz}$, where propagation loss is minimal. The initial electric field is described by

$$E_{\mathrm{in}}(t) = \mathrm{e}^{-\left(\frac{t-t_0}{\Delta t}\right)^2} \mathrm{e}^{\mathrm{i}\omega_0 t}, \quad (3)$$

where t_0 represents the delay time of pulse incidence and Δt indicates the pulse duration. The experimental setup

for injecting the time-domain pulse into the phase modulator is provided in the SM.

4. Frequency Shifting of the Spectrum. The relative range of the spectral width of the time-domain pulse and the modulation frequency of the voltage determines the output spectrum envelope. In our experiment, we used the Ceyear arbitrary waveform generator (model 1652B) to generate time-domain pulses and the Rigol arbitrary waveform generator (model DG1022) to create the modulation voltage signals. The DG1022 provided a fixed modulation frequency of $\Omega/2\pi = 8\,\mathrm{MHz}$ with a voltage range of 0 to 10 V, corresponding to the modulation period $T = 0.125\,\mu\mathrm{s}$, while the 1652B produced time-domain pulses with variable spectral widths. In the first experiment, the pulse duration was set to $\Delta t = 0.02\,\mu\mathrm{s}$, corresponding to a spectral half-width of $\Delta\omega/2\pi = 16\,\mathrm{MHz}$, where $\Delta\omega$ is defined as the half-width at $1/e$ of the pulse's peak amplitude. This pulse width is much smaller than the modulation period ($\Delta t < T/4$), as shown in Fig. 2(a). The narrow time-domain pulse width ensures that the spectral width is much broader, allowing for comprehensive modulation effects. Notably, the nonlinearity of the C–V characteristics of the varactors causes the applied voltage and the desired refractive index to deviate from a linear relation, resulting in distortion of the refractive index modulation. To address this issue, in our experiments, we measured the n–V curve and used it to map a voltage waveform that achieves a nearly ideal refractive index modulation. Detailed analysis and procedures are provided in the SM.

We precisely adjusted the phase relation between the time-domain pulse and the modulation voltage during their interaction. The experimental results, shown in Fig. 2(c), indicate that the frequency wave packet moves as a whole, exhibiting a sinusoidal trajectory. The observed frequency shift is similar to the electron packet acceleration in DLA, where the frequency-domain linear phase gradient is mapped to the accumulation of electron real-space momentum. In contrast, the theoretical spectrum evolution trajectory obtained from Eq. (2) is shown in Fig. 2(b), where the phase ϕ is scanned from 0 to 2π. The theoretical results in Fig. 2(b) and the experimental results in Fig. 2(c) display the same spectrum evolution trajectory with respect to phase ϕ, both demonstrating the characteristics of an overall spectrum shift. Specifically, frequency blue shifts occur in the phase ranges of $[0, \pi/2]$ and $[3\pi/2, 2\pi]$, while red shifts are observed in the phase interval of $[\pi/2, 3\pi/2]$. The maximum blue shift occurs at $\phi = \pi/2$, and the maximum red shift is observed at $\phi = 3\pi/2$.

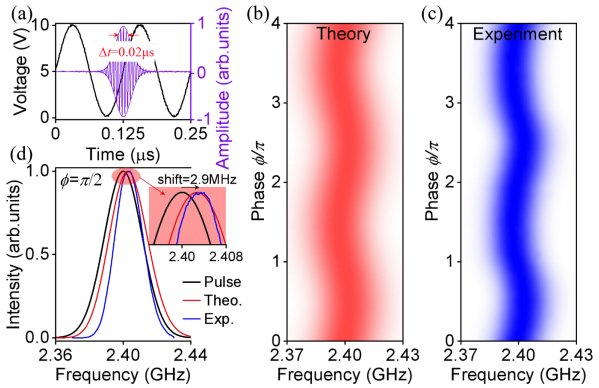

Fig. 2. An overall frequency shift. (a) The voltage modulation frequency is $\Omega/2\pi = 8\,\mathrm{MHz}$, with the pulse's time domain width $\Delta t = 0.02\,\mu\mathrm{s}$. The width is defined as half of the maximum intensity at $1/e$. (b) Spectrum shift resulting from scanning the interaction phase ϕ of the pulse and the modulation voltage. (c) Experimental observation of the spectrum shift. (d) Comparison of experimental and theoretical results at $\phi = \pi/2$, showing an output spectrum shift $\Delta f = 2.9\,\mathrm{MHz}$ relative to the incident spectrum. The inset highlights the magnified offset.

The overall frequency shift of the pulse with a sinusoidal trajectory, and the maximum spectral blue shift at $\phi = \pi/2$, are two crucial spectral features when the spectral width of the pulse is much larger than the modulation frequency. By analogy with the Schrödinger equation, we solve the nearest-neighbor coupled Hamiltonian in Eq. (1) of the spectral lattice to obtain the eigenvalues and eigenfrequencies. The initial pulse is then projected into the eigenspace composed of these eigenvectors to determine the excited photonic states in the energy band. This approach quantitatively describes the influence of the spectral width of the pulse on the distribution of photonic states within the energy band.[51,52] When $\Delta\omega$ is significantly larger than Ω, the distribution of excited photonic states in the energy band is shown in Fig. 1(e). The primary excited photonic states are located at the Brillouin center and exhibit clear linear dispersion characteristics. At $\phi = \pi/2$, when $\sin(\Omega t) \approx \Omega t$, the output field is approximately given by $E_{\mathrm{out}}(t) = \mathrm{e}^{\mathrm{i}m_\varphi \Omega t} E_{\mathrm{in}}(t)$. The corresponding output spectrum is given by

$$E_{\mathrm{out}}(\omega) = \sqrt{\pi}\Delta t\, \mathrm{e}^{-\mathrm{i}(\omega-\omega_0-m_\varphi\Omega)t_0}\, \mathrm{e}^{-\left(\frac{\omega-\omega_0-m_\varphi\Omega}{2\Delta\omega}\right)^2}. \quad (4)$$

It can be seen that the output spectrum undergoes an overall frequency shift, and the experimental value of the maximum frequency blue shift is 2.9 MHz, which is in good agreement with the 3.18 MHz given by the theoretical value $m_\varphi\Omega/2\pi$. This comparison between experiment and theory, as shown in Fig. 2(d), underscores the accuracy of our theoretical model. Noted that the maximum frequency shift value depends on the modulation depth m_φ. The SM provide simulation results for larger modulation depth values, showing frequency shifts up to 17 MHz.

5. Airy Envelope of the Spectrum. By fixing the modulation frequency Ω of the voltage and varying the duration Δt of the incident pulse, the spectral envelope of the output pulse can be effectively engineered. As the incident pulse duration increases further, falling between $T/4$ and $T/2$, the number of discrete frequency sites covered by its spectrum decreases correspondingly. The second experiment involved setting the duration of the incident pulse to $\Delta t = 0.045\,\mu\mathrm{s}$ ($\Delta\omega/2\pi = 7\,\mathrm{MHz}$), as illustrated in Fig. 3(a), which compares the time domain parameters Ω and Δt. By continuously adjusting the initial phase of the interaction, the resulting periodic frequency shift of the output spectrum is observed, as shown in Fig. 3(c). Notably, at specific phases $m\pi/2$ (where $m = 1, 3, 5, \ldots$),

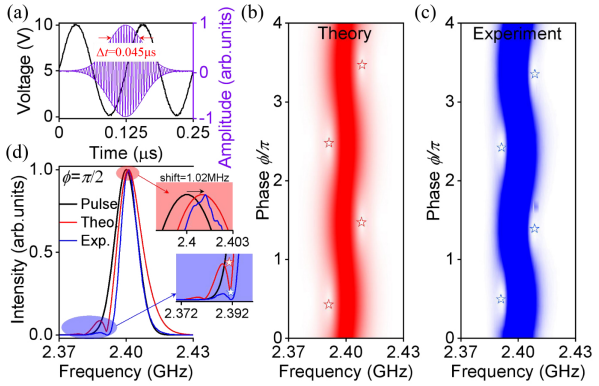

Fig. 3. Airy envelope of the spectrum. (a) Comparison of the modulation voltage and pulse, with a modulation frequency of $\Omega/2\pi = 8\,\text{MHz}$ and a pulse duration of $\Delta t = 0.045\,\mu\text{s}$. (b) Theoretical spectrum evolution obtained by varying the interaction phase of the pulse and modulation voltage, highlighting a zero point in the spectrum with a red star. (c) Experimental phase scanning of the pulse and modulation voltage, with test data points where a blue star marks the zero point in the spectrum. (d) Comparison of experimental and theoretical spectrum at $\phi = \pi/2$, showing spectrum shift and sub-lobes. The insets with red and blue backgrounds provide a magnified view of the spectrum offset and zero point values, measured at 1.02 MHz and 2.3913 GHz, respectively.

side lobes are generated, presenting a distinct difference from the overall frequency shift seen in Figs. 2(b) and 2(c). In parallel with the experimental observations, the theoretical spectrum evolution trajectory, as shown in Fig. 3(b), was derived by scanning the phase ϕ from 0 to 2π using Eq. (2). The results in theoretical Fig. 3(b) align closely with those in experimental Fig. 3(c), both exhibiting the same spectrum evolution trajectory with respect to phase ϕ. These findings not only confirm the overall spectrum shift and the emergence of side lobes but also highlight the complex interplay between phase modulation and spectral evolution.

To gain a deeper understanding of the spectral characteristics, we start by analyzing the Hamiltonian in Eq. (1) to calculate the excited photonic states within the energy band, based on the characteristic pulse width. As shown in Fig. 1(f), these excited photonic states are distributed across the energy band and are no longer confined to the Brillouin center, indicating that photonic states deviating from the Brillouin center are also excited.

When the excited region extends beyond half but does not cover the entire area, the corresponding pulse width is approximately between $T/2$ and T. Specifically, for the pulse duration Δt (the width is defined as half of the maximum intensity at $1/e$) satisfying $T/4 < \Delta t < T/2$, we can approximate $\sin(\Omega t)$ as $\Omega t - (\Omega t)^3/6$. At the phase $\phi = \pi/2$, the output field can be approximated as $E_{\text{out}}(t) = \exp\{\text{i}m_\varphi[\Omega t - \frac{(\Omega t)^3}{6}]\}E_{\text{in}}(t)$, where the phase includes both a linear term Ωt and a cubic term $(\Omega t)^3$ with respect to time t. In the first experiment, the overall frequency shift of the spectrum is primarily due to the modulation of the linear term. However, the cubic term $(\Omega t)^3$ transforms into the frequency domain through a Fourier transform, resulting in an Airy function, which satisfies the relation $\mathcal{F}^{-1}\{\exp[\text{i}(\Omega t)^3/3]\} = \text{Ai}(\omega)$. The Airy function in the frequency domain exhibits both a main lobe and side lobes, consistent with the experimental results shown in Fig. 3(c). As a result, we provide a detailed process for deriving the output spectrum in the SM, which is given in the form of

$$E_{\text{out}}(\omega) = \text{e}^{-\left(\frac{m_\varphi \Omega^3 a^3}{6} + \frac{t_0^2}{\Delta t^2}\right)} \frac{\text{e}^{-a\left(\omega_0 - \omega - \frac{2}{m_\varphi \Omega^3 \Delta t^4} + m_\varphi \Omega - \text{i}\frac{2t_0}{\Delta t^2}\right)}}{\sqrt[3]{\frac{m_\varphi}{2}}\Omega} 2\pi \cdot \text{Ai}\left(\frac{\omega_0 - \omega + m_\varphi \Omega - \frac{2}{m_\varphi \Omega^3 \Delta t^4} - \text{i}\frac{2t_0}{\Delta t^2}}{-\sqrt[3]{\frac{m_\varphi}{2}}\Omega}\right), \quad (5)$$

where $a = \frac{2}{m_\varphi \Omega^3 \Delta t^2}$ is a constant coefficient in the formula. The output spectrum exhibits both a main lobe shift and the coexistence of side lobes. The experimental value of the maximum frequency blue shift is 1.02 MHz, with the main lobe's zero position at 2.3913 GHz closely matching the theoretical value of 1.08 MHz, as well as 2.392 GHz provided by Eq. (5). This strong correlation between experiment and theory, as shown in Fig. 3(d), not only validates our theoretical model but also reinforces the consistency of our approach. Simulations and theoretical analysis indicate that higher modulation depths result in the Airy envelope developing additional side lobes. However, for longer pulse widths, the spectrum gradually deviates from the ideal Airy envelope. This deviation arises because increasing the pulse width introduces higher-order additional phase, leading to distortion. Detailed discussions are provided in the SM.

6. Airy-Type Spectral Envelope of Cubic Modulation. To experimentally demonstrate that a cubic time-dependent voltage modulation produces an Airy-type spectral envelope, a Rigol arbitrary waveform generator (DG1022) was used to apply a t^3-shaped voltage signal (based on the n–V curve mapping) to the waveguide sample. Due to equipment limitations, the modulation frequency was set at 0.5 MHz. An incident pulse with a duration of 0.2 μs was selected as shown in Fig. 4(a). After propagating once through the modulated sample, the pulse developed an Airy spectral profile, consistent with theoretical predictions, featuring a distinct main peak and clearly separated side lobes as shown in Fig. 4(b). According to theoretical analysis, the complexity and number of these side lobes depend directly on the modulation depth. Therefore, to achieve greater modulation depth, the output pulse was recirculated through the sample multiple times by collecting it at the output and feeding it back into the input port. Fig. 4(c) shows the pulse spectrum after 13 circulations, revealing an increased number of side lobes and a significant shift of the main spectral peak. This experimental result aligns closely with the theoretical model in Fig. 4(d), confirming that repeated propagation effectively enhances modulation depth and enriches the spectral structure.

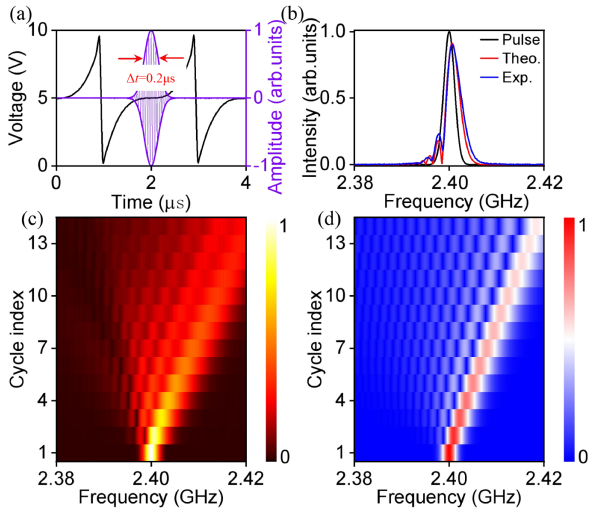

Fig. 4. Airy-type spectral envelope of cubic modulation. (a) Comparison of the cubic modulation voltage and pulse in the time domain, with a modulation frequency of $\Omega/2\pi = 0.5\,\mathrm{MHz}$ and a pulse width of $\Delta t = 0.2\,\mu\mathrm{s}$. (b) Comparison of theoretical and experimental spectrum after propagating once through the modulated sample, confirming that the Airy-function-type spectral envelope originates from cubic modulation. (c) Experimental results of spectrum evolution with the number of passes through the modulated sample. (d) Theoretical calculation of spectrum evolution.

7. Self-Healing Property of Airy-Type Spectral Envelope. In addition to its distinctive spectral shape with clear main and side lobes, the Airy function also exhibits significant self-healing properties. To experimentally demonstrate this, we captured the pulse spectrum after its second propagation through the waveguide and deliberately removed part of the main spectral lobe (the removed frequency bandwidth ∼1 MHz), as illustrated by the red curve in Fig. 5(c). The original, intact spectrum after two propagations is shown for comparison [black curve in Fig. 5(c)]. The pulse with the partially removed spectrum was then reintroduced into the waveguide for further propagation as shown in Fig. 5(a). After additional propagation (equivalent to 13 passes), experimental observations revealed that the previously removed portion of the spectrum gradually recovered [green curve in Fig. 5(c)], closely matching the spectrum of the intact pulse after the same propagation distance [blue curve in Fig. 5(c)]. This experimental result is consistent with theoretical predictions shown in Fig. 5(b), confirming the inherent self-healing capability of the Airy function. Furthermore, the formation and self-healing behavior of the Airy spectral envelope arise primarily from diffraction in the spectral domain and its intrinsic recovery properties, which provide a high tolerance to small distortions in the modulation waveform. The SM present the influence of imperfect waveforms on the formation and self-healing behavior of the Airy spectral envelope.

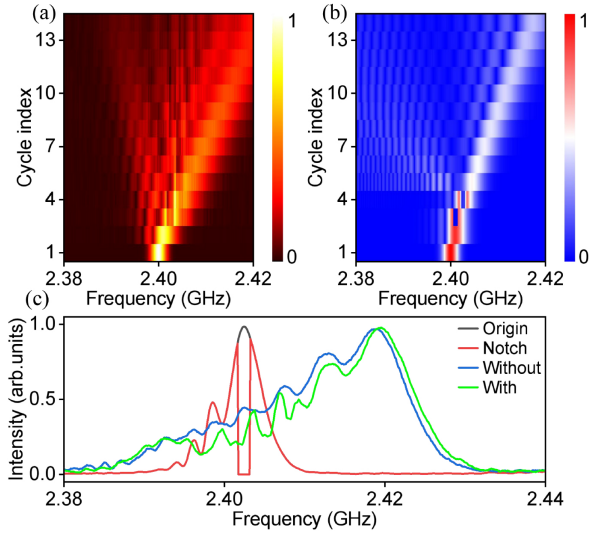

Fig. 5. Self-healing property of Airy-type spectral envelope. (a) Experimental results of the evolution of the defective spectrum with the number of sample passes. (b) Theoretical calculation of the defective spectrum evolution. (c) The black curve represents the spectral envelope of the pulse after its second pass through the sample, the red curve shows the spectral envelope with a portion of the main lobe removed, and the blue and green curves respectively depict the evolution of defect-free and defective spectral envelopes after 13 passes through the sample.

8. Discrete Spectrum Diffraction. As the incident pulse duration is further increased to $\Delta t = 0.2\,\mu\mathrm{s}$ ($\Delta\omega/2\pi = 1.5\,\mathrm{MHz}$), the pulse's spectral width becomes significantly narrower than the modulation frequency Ω ($\Delta t > T/2$), as shown in Fig. 1(d), containing only a single frequency site within the frequency band. This is also presented in Fig. 6(a), which compares the modulation period T and the pulse duration Δt in the time domain. As expected, by continuously adjusting the initial phase, symmetrical discrete sidebands are generated, as shown in Fig. 6(c). The discrete diffraction patterns closely resemble the electron–photon coupling phenomena observed in PINEM. Theoretically, the spectrum evolution trajectory is obtained by scanning the phase ϕ from 0 to 2π using Eq. (2), as illustrated in Fig. 6(b). Both the theoretical results in Fig. 6(b) and the experimental results in Fig. 6(c) reveal the same spectrum evolution trajectory with respect to phase ϕ, exhibiting the characteristics of discrete diffraction. Furthermore, based on the distribution of photonic states within the energy band, the incident time-domain pulse is sufficiently broad, causing the excited photonic states to span the entire Brillouin zone, as shown in Fig. 1(g). In contrast to the previous two regimes, where specific states of the Brillouin zone are excited, these two cases exhibit a partial excitation that shifts with changes in modulation phase. As the incident pulse becomes much longer than the modulation period, the excitation extends across the entire Brillouin zone. In this regime, the spectral response becomes largely insensitive to phase variations, as the distribution remains uniform regardless of phase. Without applying the approximation $\sin(\Omega t)$, the analytical expression for the output spectrum is given by

$$E_{\mathrm{out}}(\omega) = b\sum_{n} J_n(m_\varphi)\mathrm{e}^{-\mathrm{i}t_0(\omega-\omega_0-n\Omega)} \cdot \mathrm{e}^{-\left[\frac{\omega-\omega_0-n\Omega}{2\Delta\omega}\right]^2}, \tag{6}$$

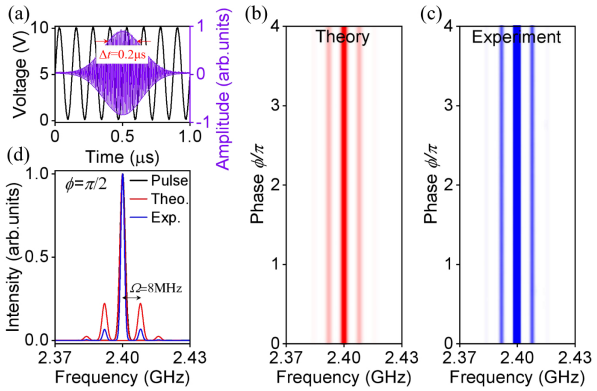

Fig. 6. Discrete frequency diffraction. (a) Comparison of modulation voltage and pulse in the time domain, with a modulation frequency of $\Omega/2\pi = 8\,\text{MHz}$ and a pulse width of $\Delta t = 0.2\,\mu\text{s}$. (b) Theoretical calculation of spectrum evolution as the interaction phase varies, showing that the spectrum remains unchanged throughout. The phenomenon is due to the pulse being wide enough that the interaction phase can no longer be precisely determined. (c) Experimental results of phase scanning for the pulse and modulation voltage, confirming that the spectrum remains constant. (d) Comparison of theoretical and experimental spectrum at $\phi = \pi/2$, highlighting that the peak interval of the spectrum corresponds to the modulation frequency Ω.

where $b = \sqrt{\pi}\Delta t e^{2t_0^2/\Delta t^2}$ is a constant coefficient in the formula. The expression indicates that the output spectrum generates symmetrical sidebands centered at ω_0, with intervals corresponding to the modulation frequency Ω. The intensity of these sidebands is determined by the modulation depth m_φ. Figure 6(d) provides a comparison between the theoretical evolution and experimental results, both of which demonstrate the intensity distribution characteristic of discrete diffraction. Simulation and theoretical results demonstrating that discrete frequency diffraction exhibits more sidebands at greater modulation depths are provided in the SM.

9. Conclusion. Our work investigates the spectral evolution of pulses in a dynamically modulated waveguide, revealing the impact of pulse duration and modulation parameters on spectral characteristics. By varying the incident pulse duration Δt and modulation frequency Ω, we observed frequency shifts, side lobes, and discrete diffraction patterns. Furthermore, by applying cubic modulation to the waveguide sample, we successfully generate an Airy-function-type spectral envelope and observe its self-healing properties. Theoretical and experimental results align, demonstrating that the spectral envelope and sideband intensity are governed by the modulation depth m_φ. These findings validate the underlying physics of synthetic dimensions and time-space regulation, providing a framework for manipulating wave packet dynamics in photonic systems. Future research will extend these concepts to more complex modulation schemes, explore non-linear effects, and develop reconfigurable photonic devices. This work lays the foundation for advancements in optical signal processing, quantum information, and the design of novel metamaterials.

We include all the following supporting information in the SM. The formal solution for phase modulation in Eq. (2); the analytical process for generating the Airy envelope from the frequency output; the impact of varactor nonlinearity on waveguide refractive index modulation and its correction; experimental setups and measurements; theoretical and COMSOL simulation results showing greater spectrum shifts at increased modulation depths; theoretical and COMSOL simulation findings indicating more sub-lobes in the Airy envelope at higher modulation depths; impact of varying pulse widths on spectral evolution at a fixed modulation frequency; the influence of imperfect waveforms on the formation and self-healing behavior of the Airy spectral envelope; theoretical and COMSOL simulation results revealing additional sidebands in discrete frequency diffraction at greater modulation depths.

Acknowledgements. Thanks to Bing Zhang from Tel Aviv University for helpful discussions in the derivation of the formula. Q. Cheng was supported by the National Natural Science Foundation of China (Grant No. 12174260), the Shanghai Rising-Star Program (Grant No. 21QA1406400), and the Shanghai Science and Technology Development Fund (Grant Nos. 21ZR1443500 and 21ZR1443600). C. Wang was supported by Research Grants Council, University Grants Committee (Grant Nos. STG3/E-704/23-N, CityU 11212721, and CityU 11204523).

References

[1] Yuan L Q, Lin Q, Xiao M, and Fan S H 2018 *Optica* **5** 1396
[2] Lu L, Joannopoulos J D, and Soljačić M 2014 *Nat. Photonics* **8** 821
[3] Ozawa T and Price H M 2019 *Nat. Rev. Phys.* **1** 349
[4] Lustig E and Segev M 2021 *Adv. Opt. Photonics* **13** 426
[5] Ozawa T, Price H M, Goldman N, Zilberberg O, and Carusotto I 2016 *Phys. Rev. A* **93** 043827
[6] Bell B A, Wang K, Solntsev A S, Neshev D N, Sukhorukov A A, and Eggleton B J 2017 *Optica* **4** 1433
[7] Luo X W, Zhou X, Li C F, Xu J S, Guo G C, and Zhou Z W 2015 *Nat. Commun.* **6** 7704
[8] Regensburger A, Bersch C, Miri M A, Onishchukov G, Christodoulides D N, and Peschel U 2012 *Nature* **488** 167
[9] Boada O, Celi A, Latorre J, and Lewenstein M 2012 *Phys. Rev. Lett.* **108** 133001
[10] Gadway B 2015 *Phys. Rev. A* **92** 043606
[11] Yuan L Q, Shi Y, and Fan S H 2016 *Opt. Lett.* **41** 741
[12] Lustig E, Weimann S, Plotnik Y, Lumer Y, Bandres M A, Szameit A, and Segev M 2019 *Nature* **567** 356
[13] Regensburger A, Bersch C, Hinrichs B, Onishchukov G, Schreiber A, Silberhorn C, and Peschel U 2011 *Phys. Rev. Lett.* **107** 233902
[14] Maczewsky L J, Wang K, Dovgiy A A, Miroshnichenko A E, Moroz A, Ehrhardt M, Heinrich M, Christodoulides D N, Szameit A, and Sukhorukov A A 2020 *Nat. Photonics* **14** 76
[15] Wang K, Bell B A, Solntsev A S, Neshev D N, Eggleton B J, and Sukhorukov A A 2020 *Light Sci. Appl.* **9** 132
[16] Zhang M, Buscaino B, Wang C, Shams-Ansari A, Reimer C, Zhu R, Kahn J M, and Lončar M 2019 *Nature* **568** 373
[17] Wang C, Zhang M, Chen X, Bertrand M, Shams-Ansari A Chandrasekhar S, Winzer P, and Lončar M 2018 *Nature* **562** 101

[18] Wang C, Li Z, Kim M H, Xiong X, Ren X F, Guo G C, Yu N, and Lončar M 2017 *Nat. Commun.* **8** 2098
[19] Wang C, Zhang M, Yu M J, Zhu R R, Hu H, and Loncar M 2019 *Nat. Commun.* **10** 978
[20] Upreti L K, Evain C, Randoux S, Suret P, Amo A, and Delplace P 2020 *Phys. Rev. Lett.* **125** 186804
[21] Vatnik I D, Tikan A, Onishchukov G, Churkin D V, and Sukhorukov A A 2017 *Sci. Rep.* **7** 4301
[22] Yuan L Q and Fan S H 2016 *Optica* **3** 1014
[23] Lin Q, Xiao M, Yuan L Q, and Fan S H 2016 *Nat. Commun.* **7** 13731
[24] Zhang Y and Zhu Y Y 2017 *Phys. Rev. A* **96** 013811
[25] Rechtsman M C, Zeuner J M, Plotnik Y, Lumer Y, Podolsky D, Dreisow F, Nolte S, Segev M, and Szameit A 2013 *Nature* **496** 196
[26] Gover A and Pan Y M 2018 *Phys. Lett. A* **382** 1550
[27] Pan Y M and Gover A 2019 *Phys. Rev. A* **99** 052107
[28] Peralta E, Soong K, England R *et al.* 2013 *Nature* **503** 91
[29] England R J, Noble R J, Bane K *et al.* 2014 *Rev. Mod. Phys.* **86** 1337
[30] Breuer J and Hommelhoff P 2013 *Phys. Rev. Lett.* **111** 134803
[31] Park S T, Lin M, and Zewail A H 2010 *New J. Phys.* **12** 123028
[32] Pan Y M, Zhang B, and Gover A 2019 *Phys. Rev. Lett.* **122** 183204
[33] Barwick B, Flannigan D J, and Zewail A H 2009 *Nature* **462** 902
[34] Roberts C, Schmidt S, and Vinnik D 2002 *Phys. Rev. Lett.* **89** 153901
[35] Man Z X, Xia Y J, and An N B 2017 *Sci. Rep.* **7** 42539
[36] Morin O, Huang K, Liu J L, Le J, Han N, Fabre C, and Laurat J 2014 *Nat. Photonics* **8** 570
[37] Kolesov R, Grotz B, Balasubramanian G, Stöhr R J, Nicolet A A, Hemmer P R, Jelezko F, and Wrachtrup J 2009 *Nat. Phys.* **5** 470
[38] Kong G S, Ma H F, Cai B G, and Cui T J 2016 *Sci. Rep.* **6** 29600
[39] Zhang J J, Zhang H C, Gao X X, Zhang L P, Niu L Y, He P H, and Cui T J 2019 *Sci. Bull.* **64** 843
[40] Garcia-Vidal F J, Fernández-Domínguez A I, Martin-Moreno L, Zhang H C, Tang W, Peng R, and Cui T J 2022 *Rev. Mod. Phys.* **94** 025004
[41] Andersen O K and Jepsen O 1984 *Phys. Rev. Lett.* **53** 2571
[42] Ibanez-Azpiroz J, Eiguren A, Bergara A, Pettini G, and Modugno M 2013 *Phys. Rev. A* **87** 011602
[43] Ortenzi L, Cappelluti E, and Pietronero L 2016 *Phys. Rev. B* **94** 064507
[44] Reinhardt O and Kaminer I 2020 *ACS Photonics* **7** 2859
[45] Dahan R, Nehemia S, Shentcis M *et al.* 2020 *Nat. Phys.* **16** 1123
[46] Qin C Z, Zhou F, Peng Y G, Sounas D, Zhu X F, Wang B, Dong J J, Zhang X L, Alù A, and Lu P X 2018 *Phys. Rev. Lett.* **120** 133901
[47] Huang W P and Mu J W 2009 *Opt. Express* **17** 19134
[48] Martijn de Sterke C and Sipe J E 1990 *Phys. Rev. A* **42** 550
[49] Hall D G 1990 *Opt. Lett.* **15** 619
[50] Bowen P T and Smith David R 2014 *Phys. Rev. B* **90** 195402
[51] Mandelik D, Eisenberg H, Silberberg Y, Morandotti R, and Aitchison J 2003 *Phys. Rev. Lett.* **90** 053902
[52] Xu B B, Li T, and Zhu S N 2018 *Opt. Express* **26** 13416